Title

THE INFLUENCE OF OXYGEN ON SEGREGATION OF CHROMIUM AT STRUCTURAL DAMAGE IN GALLIUM ARSENIDE

Author

Zee, T.I.S.-Y.

Publication Date

1983-06-01

Lawrence Berkeley Laboratory
UNIVERSITY OF CALIFORNIA

Materials & Molecular Research Division

THE INFLUENCE OF OXYGEN ON SEGREGATION OF CHROMIUM AT STRUCTURAL DAMAGE IN GALLIUM ARSENIDE

T.I.S.-Y. Zee
(M.S. Thesis)

June 1983

Prepared for the U.S. Department of Energy under Contract DE-AC03-76SF00098

DISCLAIMER

THE INFLUENCE OF OXYGEN ON SEGREGATION OF CHROMIUM AT STRUCTURAL DAMAGE IN GALLIUM ARSENIDE

Terry Ivy Sun-Yu Zee

Lawrence Berkeley Laboratory
Department of Materials Science and Mineral Engineering
University of California
Berkeley, California

This work was supported by the Director, Office of Energy Research, Office of Health and Environmental Research of the U.S. Department of Energy under Contract No. DE-AC03-76SF00098.

TO MY BELOVED HUSBAND

WHO HAS GIVEN ME HIS EMOTIONAL SUPPORT,
CONSTANT ENCOURAGEMENT, AND PERMISSION
TO MAKE THIS WORK POSSIBLE

WITH LOVE I DEDICATE THIS

THE INFLUENCE OF OXYGEN ON SEGREGATION OF CHROMIUM AT STRUCTURAL DAMAGE IN GALLIUM ARSENIDE

Terry Ivy Sun-Yu Zee

Lawrence Berkeley Laboratory
Department of Materials Science and Mineral Engineering
University of California
Berkeley, California

ABSTRACT

The redistribution of Cr in the presence of dislocations and O atoms in ion implanted and subsequently furnace annealed GaAs has been studied by cross-sectional TEM (XTEM) and Secondary Ion Mass Spectrometry (SIMS). Cr-doped, semi-insulating (100) GaAs samples were self implanted with 550 keV Ga and As ions at room temperature (RT). To illustrate the role of O in the redistribution process, two different doses ($4x10^{13}$ cm^{-2} and $2x10^{15}$ cm^{-2}) of O were also implanted after the implantation of the above ions. The initial implantation damage in samples with or without oxygen consisted of continuous bands of amorphous and microtwinned material, respectively. Comparison of the TEM results from annealed samples (600-840°C) with and without O showed that highly twinned and misoriented GaAs forms along with a network of densely entangled dislocations near the surface ($0-R_p$) in the former case while only entangled dislocations by plastic deformation occur over the depth range $0-R_p$ in the latter case. The deeper parts in both cases contained bands of dislocation loops, the mean diameter of which became progressively smaller with increasing amount of O. SIMS analysis showed that remarkable

redistribution of Cr and O occur in the implanted region and its vicinity. In the samples without O, there was a one to one correspondence between the positions of the damage layers and peaks in the atomic profile of Cr. However, in the presence of O such correlations became complicated. A qualitative model explaining the redistribution behavior of Cr in amorphous GaAs and Cr segregation to the defects has been presented. The pronounced effect of O on Cr redistribution and retardation in the annealing out of dislocations has been explained by considering the formation of Cr-O complexes during the annealing and their interaction with dislocations.

INTRODUCTION

Ion implantation is a high energy physical process of introducing charged atomic particles in a controlled manner into a substrate for the purpose of modifying its electrical, mechanical, chemical, and metallurgical properties. The initial depth profiles of the implanted ion and damage depend primarily on the energy of the incident beam, the implanted ion dose, the atomic mass and atomic number of the projectile. Provided that the ion beam is incident at an angle $\geq 5^{\circ}$ from a major crystallographic axis, the spatial distribution of the implanted ion assumes an approximate Gaussian distribution. The mean perpendicular distance of the implanted ion beneath the surface, R_p, otherwise known as the projected range (see Fig. 17), is found to be a function of the incident ion beam energy, while ΔR_p, the width of the damage band varies directly with the ion dose.

Both R_p and ΔR_p can be calculated for any ion species and substrate with reasonable accuracy by the LSS (Lindhard, Scharff and Schiott) theory.[1] For deeply penetrating ions, a "tail" in the distribution is usually observed. This "channeling" effect has been attributed to enhanced diffusion due to the presence of large numbers of interstitial implanted ion and/or scattering of impinging ion into preferred crystallographic directions.[2]

An obvious advantage of ion implantation in device fabrication is reproducibility from run to run as well as uniformity of the device characteristics. However, damage is inevitably produced by this violent process. As the impinging ion enters the material, target

atoms in the host lattice are displaced from their proper sites. These collisions cause the clustering of excess vacancies near the surface and interstitials, which consist of deflected host atoms and impinging ions, deeper in the material.[3]

The formation and nature of damage structures in ion implanted Si and GaAs have been extensively studied.[4-6] The width of the damage layer under particular ion implantation conditions depends on the ion dose. For a given peak concentration of implanted ion, a higher dose would yield a wider amorphous layer than that resulting from the lower dose.[7] A comparison between the theoretical profile of damage and actual experimental ion distribution shows that the peak of damage distribution is closer to the surface by a factor of 0.7 than that of the ion distribution (Fig. 18).[8] The dependence of the nature of damage structures formed on implantation temperature for a fixed dose has also been studied.[5,6] At low implantation temperature (for example liquid nitrogen temperature) where mobility of interstitial atoms is low and all atomic displacements are frozen in, wider amorphous layers are created as compared to the room temperature implants. As temperature increases, considerable dynamic annealing takes place during implantation and fine crystalline regions may be present in the amorphous layer. With $5 \times 10^{14}/cm^2$ at room temperature, $10^{15}/cm^2$ at 150°C and $5 \times 10^{15} cm^2$ at 350°C, different damage structures were obtained in 120 keV P^+ implanted Si.[7] They were a buried amorphous layer, a continuous amorphous layer extending from the surface, and a buried layer of clusters

parallel to specimen surface, respectively. The amorphous/damage material formed by ion implantation is electrically inactive and subsequent annealing is necessary to achieve electrical activity. The regrowth behavior of ion-implantation induced damage layers in both Si and GaAs have been investigated by many workers.[7,9-14] The geometry and type of secondary defects left after subsequent furnace annealing depend critically on implantation conditions.[11,15]

An interface region exists between the amorphized region and the damaged but still crystalline region. During annealing, regrowth begins from this interface towards the amorphous region. If the starting damage configuration consisted of a continuous amorphous layer extending to the specimen surface, the resulting damage after subsequent furnace annealing consisted of high density of twin lamellae, dislocation network and dislocation loops.[3] In the case of a buried amorphous layer, annealing causes the formation of two layers of interstitial loops. Vacancies near the surface left behind by the collision of the incoming implant atoms with host atoms cluster together upon annealing and form stacking fault tetrahedra. Although recrystallization occurs during annealing at ~200°C in GaAs, secondary defect structures persist even at higher annealing temperature ($\geq$800°C). These defects may be electrically active or may act as sinks for migrating impurity ions. Previous work have established that the presence of defects and impurities and their interactions in both Si and GaAs causes a decrease in minority carrier lifetime, carrier removal and mobility degradation.[1,3,9-13,15-21] Among the many

impurities, Cr has been rather extensively studied[22-27] because of its high diffusion rate and low solid solubility. Under commonly used annealing conditions, Cr accumulates in regions of stress and high defect density.[26] In early stages of annealing, Cr is localized at $R_p + \Delta R_p$. Its concentration increases as defect density increase in this region, suggesting a damage gettering mechanism occurring during the annealing process.

The redistribution of Cr during the annealing of implants in semi-insulating GaAs has important consequences in the fabrication of reliable microwave field effect transistors and integrated circuits. Cr accumulation in vapor phase epitaxial growth (VPE) or active regions can cause inconsistent channel mobilities in FETs and degrade the long-term device reliability. To prevent and control Cr redistribution into undesired regions, various attempts have been made. The insertion of a GaAs buffer layer between the substrate and active layer formed by ion implantation or diffusion was adopted to reduce the Cr out-diffusion from substrate into the active layer.[28] The use of buffer layers have been a subject of much research recently. Nozaki et al.[29] first showed that the introduction of a buffer layer increased the mobility of electron in the active layer near the pinch off point. This result has been verified by many workers, but the growth of buffer layers on semi insulating substrates is a difficult process. Furthermore, after annealing at temperature above ~700°C, Cr was found to diffuse readily into the VPE layer.[28]

The introduction of mechanical damage at the back surface of the specimen has also been explored.[22,30,31] Though the presence of a

high density of dislocations at the back surface considerably reduces the out diffusion of Cr in the epitaxial layer, it was found that at higher annealing temperature ($\geq$800°C) and/or longer annealing time ($\geq$4 hours), damage annihilation accelerates and no noticeable improvement was obtained by this gettering technique.

Stress induced by an encapsulant layer (SiO_2 or Si_3N_4) constitutes another possible gettering mechanism for impurities in GaAs substrates, and has also been suggested to account for Cr out diffusion to the surface.

The redistribution of Cr and its interaction with defects, and the formation of its complexes with other impurities in GaAs is presently not well understood. The goal of the work is to combine the SIMS and XTEM techniques to study the role of dislocations and oxygen in Cr redistribution in ion implanted and subsequently furnace annealed GaAs. For ion implantation, Ga and As ions were chosen to avoid chemical affinity effects on Cr redistribution. A variety of defect structures were created on subsequent annealing of high dose (10^{15} cm^{-2}) implantation of the above ions. Oxygen was also introduced by implantation into the amorphized surface layers to study its effect on Cr redistribution. Depth distribution of structural defects, Cr and O profiles were obtained by XTEM and SIMS, respectively, from the same set of samples. Using this approach, direct depth correlations could be made between Cr, O, and structural defects.

EXPERIMENTAL

A. Sample Preparation

1) Ion Implantation. Semi-insulating, Cr-doped, horizontal bridgeman GaAs wafers were used as the starting material. To create damage in the substrate, Ga and As were implanted at 550 and 575 kev, respectively, into the polished surface of (100) GaAs at room temperature. Two different implantation energies were employed to match the projected range of the two ions. Each ion dose was 5×10^{14} cm^{-2}, making a total of 10^{15} cm^{-2}.

To study the effect of oxygen on Cr redistribution and damage annealing, oxygen was implanted in a non-channeling direction into the GaAs wafer at energies of 80 and 240 kev consecutively. The dual-energy oxygen implant was adopted to achieve a more uniform concentration of oxygen with depth. In the presence of a 2000 Å SiO_2 encapsulant, these energies theoretically corresponded to an implant projected range of 2000 Å in the GaAs substrate. Two different fluences of oxygen were chosen - the lower dose was 4×10^{13} and the higher one was 2×10^{15} cm^{-2}. Samples with these respective oxygen implant fluences will be referred to in the text from here on as low fluence and high fluence samples. The control sample represents the one without an additional oxygen implant.

2) Capping. As subsequent annealing generally induces surface decomposition of GaAs with the loss of As, the damaged wafers were capped with 2000 Å of silicon dioxide at 410°C by the chemical vapor deposition method. This capping also served to minimize surface degradation or reaction with gaseous impurities.

3) Annealing. In order to reduce the implant-induced lattice disorder and to recover crystallinity, subsequent furnace annealing in the temperature range of 600°C to 840°C was carried out. In some cases, a dual anneal of 600°C followed by a 840°C anneal was also performed. The annealing time varied from 15 minutes to 40 minutes. All anneals except one were carried out in a N_2 atmosphere. This exceptional one was allowed to anneal in air at 600°C for 40 minutes.

B. TEM Specimen Preparation

1. Plan-View Specimens. Specimens with dimensions of approximately 2mm x 2mm were cut out from the processed wafer. Each specimen was thinned mechanically from the unimplanted side only using progressively finer grit size SiC paper until the specimen thickness approached ~100 micron. A 6-micron diamond paste was used for final polishing. The mechanically polished specimen was subsequently chemical jet thinned from the unimplanted side using a chlorine-methanol solution. This solution was prepared by allowing the chlorine to bubble through some methyl alcohol. Both the chlorine concentration in the solution and the velocity of the solution as it touched the specimen surface were vital to obtain a large thin area for the TEM analysis. During chemical thinning, the specimens were rotated to ensure uniform etching. As soon as a hole appeared, the specimen was removed and immersed in water and etching terminated. After cleansing, the thinned specimens were mounted onto 3mm brass rings for TEM analysis. Silver paste was applied at contact points to prevent charging up of the specimen surface. Finally, the SiO_2 cap on the

surface was removed by dipping the mounted specimen in 48 percent hydrofluoric acid for roughly 15 seconds.

2) 90° Cross-Section Specimens. Initial mechanical thinning was done on specimens obtained by cleaving along a <110> cleavage direction from the processed wafer. The specimen was glued face to face to a slightly larger piece of silicon with contact adhesive. This was done for identification purpose. The two pieces were then mounted on a glass disc with wax with a piece of silicon placed on either side for support. The surface was polished flat with 600 grit SiC paper followed by a 6-micron diamond paste to improve the surface finish. The specimen was then turned over, remounted with wax, and the polishing sequence repeated to give a final specimen thickness of less than 25 micron. As the integrity of the implanted surface is vital to later analysis of existing microstructures, care was taken to maintain the abrasive wheel spinning in a direction away from the implanted surface. Subsequent thinning was performed using a 6kV, 50μA Ar^+ ion beam. The specimen was mounted with the mechanically polished surface making an angle of ~20° with the ion beam. It was oriented with the edge of interest furthest from the ion-gun and thinned from one side at a time. After thinning for approximately one hour on one side, it was turned over and thinned from the second side until penetration occured at the edge. To improve the quality of the specimen, it is important to start with a rather thin mechanically polished specimen before ion milling. The finished specimen was mounted onto a 3mm brass ring for later TEM analysis (Fig. 2b).

C. SIMS Measurement

The Cr and oxygen distributions in the same sample were measured by secondary ion mass spectrometry (SIMS) using O^- ion and Cs^+ ion bombardment, respectively. The combination of SIMS data and the exact knowledge of the fluence of the implanted ion gave the absolute atomic concentration in the implanted specimen.

The existence of a surface oxide can have strong effect on the observed secondary ion signals. Therefore, the SiO_2 cap in all samples were removed by dissolution in an HF solution before the SIMS analysis. A detailed description of the SIMS technique has been presented by Newburg.[32]

D. TEM Analysis

TEM studies of defect structures were made using "plan view" and "90° cross-sectional" specimens. Such examination allows the determination of both the general nature and three dimensional distribution of the damage. All analysis was done using the bright field diffraction imaging technique on a Phillips 400 Electron Microscope or a JEM 100C. Diffraction patterns were recorded in certain cases to verify the crystallinity of the damaged surface layer.

RESULTS AND DISCUSSION

To make depth comparisons between visible damage bands and the Cr and O distributions in the specimen, the magnification of each cross-section micrograph was matched with its corresponding SIMS depth profile for Cr and O. Since the experiments were designed to study the effect of O on Cr redistribution, the results are presented in three

parts: 1) a control specimen in which no O was intentionally introduced, 2) a specimen in which O was implanted into the surface layers to a fluence of $4 \times 10^{13}/cm^2$ and, 3) a specimen with O implanted to $2 \times 10^{15}/cm^2$.

The depth distributions of damage regions, and of Cr and O peaks have been tabulated (Table 1) to facilitate cross-referencing. For wide defect layers, the lower and upper bounds of the band are provided. If the damage layer had a non-uniform or graduated distribution of defects, the position of maximum defect density has also been recorded. Magnitudes of the peaks for the SIMS measurements are also shown. Lines are drawn between sets of data which were considered to demonstrate possible correlations.

Since no oxygen had been implanted in the control specimens, oxygen atomic concentrations were not measured for that sequence.

Control specimens (Implanted with Ga and As only). For the as-implanted specimen, the cross-sectioo micrograph (Fig. 1b) shows a uniform band of heavily damaged material continuous from the surface to a depth of ~0.28 μm. The inner edge of the band was not well defined, and small clusters of visible damage were present immediately beneath the band edge. These extended for some distance into the interior of the material. The plan-view micrograph (Fig. 1a) shows a fine dotty structure while the TED pattern from a thin region of the plan-view specimen consisted of continuous, diffuse rings indicating that the surface damage contained amorphous material. The atomic profile of Cr was a horizontal line indicating that the distribution of Cr in the material was uniform with depth.

TABLE 1. Depth Distribution of Defect, Cr, and O.

Annealing Temp.	Annealing Duration	Oxygen Fluence (cm^{-2})	Damage Layers position from surface in μm				Magnitude of Cr peaks (No. of atoms/cm^3) position from surface in μm					Magnitude of O Peaks (No. of atoms/cm) position from surface in μm			
			0.28												
600°	15'	None	0-0.2	0.27	0.34 0.32-0.44		[2.3E17] 0.135	[3.2E17] 0.29		[2.2E17] 0.40	[1.6E17] 0.6	[2.2E17] 0.77			
	40'	None	0-0.17	0.25	0.33 0.3-0.45	0.6	[2.3E17] 0.14	[4.0E17] 0.30		[1.9E17] 0.40	[1.95E17] 0.57	[2.0E17] 0.80			
(Air) 600°	40'	None	0-0.18		0.45 0.25-0.5	0.6	[6.6E17] 0.17			[2.3E17] 0.46	[1.4E17] 0.67	[1.3E17] 0.95	[1.0E20] 0.06		
840°	15'	None	0-0.15		0.36 0.25-0.46		[4.2E17] 0.20			[1.7E17] 0.40		[1.5E17] 0.92			
600°	15'	$4x10^{13}$	0-0.2		0.32 0.25-0.46		[1.6E17] 0.20	[2.0E17] 0.31		[2.8E17] 0.38	[2.0E17] 0.50			[1.2E18] 0.15	[6.4F18] 0.52
600° + 840°	15'+15'	$4x10^{13}$	0-0.14	0.285	0.35-0.45		[2.2E17] 0.175	[2.8E17] 0.31		[5E17] 0.41	[6E16] 0.56		[2.8E19] 0.06		[1.5E18] 0.50
840°	15'	$4x10^{13}$	0-0.04		0.3-0.52		[2.3E17] 0.17	[2.4E17] 0.26	[3E17] 0.32	5.2E17 0.41	[6E16] 0.53		[9E18] 0.05		[1.5E18] 0.45
		$2x10^{15}$	0.30											0.125	0.56
600°	15'	$2x10^{15}$	0-0.28		0.36 0.3-0.53		[2E17] 0.18	[2.4E17] 0.36		[2.2E17] 0.45	[2.9E17] 0.71	[1.2E17] 1.0	[4.2E19] 0.08	[4E19] 0.32	[1E19] 0.8
600° + 840°	15'+15'		0-0.25		0.39-0.57		[2.7E17] 0.21	[5E17] 0.35		[2.4E17] 0.45	[1.4E18] 0.66		[4.5E19] 0.08	[3.4E19] 0.26	[2.3E19] 0.47	[1.9E19] 0.73
840°	15'	$2x10^{15}$	0-0.2		0.32-0.52	0.6	[2.5E17] 0.21	[3.7E17] 0.34		[2.4E17] 0.42	[2.9E18] 0.61		[5.4E19] 0.075	[3.5E19] 0.23	[2.4E19] 0.42	[2.0E19] 0.68

Subsequent annealing of the sample at 600°C for 15 minutes in a nitrogen atmosphere resulted in a complicated distribution of defects (Fig. 2a). Three distinct damage layers, D_1, D_2, and D_3 were observed. D_1 contained entangled dislocations looping from the surface to a depth of 0.2 μm. D_2 consisted of a very narrow layer of small dislocation loops, lying at a mean depth of 0.27 μm. D_3 was a band of small damage clusters, extending from 0.32 μm to 0.44 μm. The plan-view micrograph (Fig. 3a) revealed only a dense tangle of dislocations. No loops from the two underlying layers were clearly visible. The Cr atomic distribution from a different area of the same sample showed three peaks C_1, C_2, and C_3 at depths 0.135 μm, 0.29 μm, and 0.4 μm, respectively (Fig. 2b). All Cr peaks corresponded closely to the locations of high defect density regions as seen on the XTEM micrograph. However, no obvious defect structure was found on the micrograph which matched the small Cr shoulders S_1 and S_2 which appeared at 0.6 μm and 0.77 μm from the surface.

Longer annealing at 600°C for a total of 40 minutes produced similar results. The cross-section micrograph (Fig. 4a) again showed three damage layers similar to those observed in the sample annealed for 15 minutes. In this case, the surface damage layer contained long looping dislocation lines, while the dislocation loops and damage clusters of the underlying layers had all increased in size. In agreement with the XTEM micrograph, the plan-view micrograph (Fig. 5a) showed a marked reduction in dislocation density. The Cr atomic profile (Fig. 4b) showed four peaks at 0.14 μm, 0.3 μm, 0.4 μm, and

0.57 μm, respectively. The first three Cr peaks C_1, C_2 and C_3 corresponded very well with high dislocation density positions. At the position of the last Cr peak, C_4, small scattered damage clusters were observed.

When nitrogen was replaced by air during the annealing of a similar but uncapped sample, the cross-section micrograph (Fig. 6a) showed only two discrete defect layers. The first layer consisted of dense dislocation tangles stretching from the surface to a depth of 0.18 μm. The second layer consisted of an 0.2 μm wide band of small dislocation loops of varying dimensions (from 0.26 μm to 0.46 μm). The Cr atomic profile (Fig. 6b) showed three peaks. The first two peaks at 0.17 μm and 0.46 μm were both located at the inner edges of the two damage layers. No visible defect structure was found which corresponded to the third Cr peak that occurred at 0.67 μm from the specimen surface or the Cr shoulder at 0.95 μm. The oxygen profile showed a single peak lying within the surface damage. The corresponding plan-view micrograph showed two layers of distinctly different structures (Fig. 5b). The surface layer was polycrystalline while the layer beneath it showed a complicated structure with no recognizable defect features. Oxidation has probably taken place.

The cross-section micrograph from the control sample after annealing at 840°C showed only one major layer of damage at a mean depth of 0.3 μm. (Fig. 7a). The surface damage had almost completely disappeared. Only a few single dislocations were found looping from the specimen surface. The Cr atomic distribution from a different area

of the same sample showed two distinct peaks C_1 and C_2 (Fig. 7b). C_2 lay near the inner edge of the major damage layer whereas no visible damage was seen which corresponded to the first Cr peak C_1.

The Cr atomic concentration profiles revealed by SIMS measurement corresponded very well with positions of defect bands. In every case, distinct Cr peaks were found lying at the inner edge of the surface damage band and interior damage bands. Though the surface damage band disappeared with the increase in annealing temperature, Cr atoms remained relatively at the same location, marking the initial inner edge of the band.

Residual damage was found to extend to distances much greater than predicted theoretically by LSS curves. The reason for such deep penetration of damage into the material is probably associated with high mobility of point defects in GaAs and channeling of the ions that occurred during the implantation. Previous studies have shown that in Si, this damage clusters to form interstitial dislocation loops.

Specimens with Implanted Oxygen

1) Low fluence specimens. (Implanted with Ga, As, and $4\times10^{13}cm^{-2}$ oxygen). After annealing at 600°C, two major damage bands were found (Fig. 8a). The surface damage extending to a mean depth of 0.2 μm was composed of extremely dense dislocation tangles. The inner edge of the band was again not well defined. At ~0.05 μm away, another significant damage layer began. This band extended all the way to 0.46 μm and was composed of dense damage clusters. The Cr distribution was almost uniform. Two small peaks, C_1 and C_2, and

two shoulders, S_1 and S_2, could still be identified (Fig. 8b). C_1, at 0.2 μm from the surface, marked the precise location of the inner edge of the surface damage band. C_2, again within the buried second damage layer, was slightly displaced towards its inner edge. The first shoulder coincided with the start of the second damage band while the second shoulder, S_2, was beyond the inner edge of this band where no visible defects were found. The oxygen profile showed a high surface concentration with a small shoulder O_1 at the tail of the surface damage band and a peak O_2 at 0.52 μm from the surface that coincided with the position of the second Cr shoulder (Fig. 8b). There was no one-to-one correlation between the damage and oxygen profile.

After dual annealing at 600°C and 840°C, two distinct damage layers were still observed (Fig. 9a). The surface damage slightly reduced in width, but still contained a high density of dislocation tangles. The second damage layer at a mean depth of 0.4 μm was drastically reduced in defect density and contained only a few dislocation loops of diameter up to ~500 Å. Small damage clusters were detected in the region between the two major defect bands. These corresponded very well with the existence of the two Cr shoulders. High Cr concentration at the specimen surface was again recorded. An overall high plateau of Cr was found in the neighborhood of damage regions. Two Cr peaks, C_1 and C_2 (Fig. 9b) occurred at the two ends of the plateau. C_1 marked the end of the surface damage while C_2 was located near the inner edge of the interior damage layer. Another Cr shoulder at 0.56 μm was recorded before Cr concentration

reached the bulk level. The oxygen profile showed two distinct peaks O_1 and O_2. One corresponded to the surface high defect concentration while the other lay between the last Cr peak and shoulder.

After annealing at 840°C, surface damage band rapidly annealed out leaving behind only a thin layer of defects at the surface. The band of interior damage still consisted of dislocation loops which had increased to a maximum diameter of ~750 Å. The shapes of both O and Cr profiles remained relatively the same as in the case of the dual temperature annealing. But Cr peaks were found to have slightly shifted towards the interior and had assumed a better correlation with the oxygen peaks.

In general, the low fluence oxygen implanted specimens followed a similar behavior pattern to the control specimens. Two major damage bands were observed at each annealing temperature. Again, a good qualitative correlation between high Cr concentration and high defect density regions was obtained.

2. High fluence specimens (Implanted with Ga, As and $2x10^{15}cm^{-2}$ oxygen). The as-implanted sample had a similar but slightly wider band of surface damage than the unannealed control sample (Table 1). The corresponding plan-view micrograph (Fig. 11a) shows a relatively complicated structure. The striations within the damage band on the XTEM micrograph gives evidence of slip on (111) planes during formation of the damage band. The TED pattern (Fig. 11a insert) showed a single crystal spot together with sharp discontinuous rings and many satellite spots indicating that preferred orientation

polycrystalline material and microtwins were present. The Cr atomic profile appeared as a straight line showing that initially there had been a uniform distribution of Cr with respect to depth. The as-implanted specimen showed two oxygen peaks (within the surface damage). One appeared at the surface damage and the other lay at ~0.56 μm from the surface where no visible defects were present.

Subsequent annealing at 600°C formed two distinct damage layers (Fig. 13a). The surface damage, though slightly narrower after annealing, still retained heavy damage. At ~0.05 μm away, a broad band of small damage clusters was observed. Its density gradually decreased as it went deeper into the material. The Cr atomic profile was almost flat. Only very small peaks and shoulders were noticed. Relatively higher Cr concentration at the surface was again detected. Corresponding to locations of the two damage layers only a shoulder and a small peak of Cr was found. A comparatively larger Cr peak occurred where an oxygen peak was present. The oxygen atomic profile showed three peaks; O_1 at the surface, O_2 lay where small damage clusters began to scatter, and O_3 at 0.8 μm where no visible defect was observed (Fig. 13b).

After the dual temperature annealing, the surface damage still contained dense dislocation tangles. Though in some portions damage was annealed out, heavily damaged material still existed (Fig. 14a). The buried band of small damage clusters, however, became much narrower and dislocation loops were seen at a mean depth of 0.43 μm. The Cr atomic profile developed three distinct peaks in addition to the usual

high surface concentration (Fig. 14b). The first peak C_1 occurred at the inner edge of the surface damage. The second peak, C_2, lay at the edge of the band of buried dislocation loops on the side nearer to the specimen surface while a small Cr shoulder occurred at the other edge. A pronounced Cr peak was detected well into the bulk at ~0.66 μm. No damage was seen at that depth. The oxygen profile consisted of four peaks of decreasing magnitude from the surface (Fig. 14b). The peak O_1 corresponded with the position of the surface damage while O_3 matched very well with the buried layer of dislocation loops. The peaks O_2 and O_4 which did not correspond to any damage layer stayed at roughly the same positions as the two oxygen peaks detected after the 600°C anneal, but this time slightly shifted to the exterior.

After a direct 840°C anneal, both damage layers still remained (Fig. 15a). The surface damage extended to a considerable depth (0.2 μm) and a large number of dislocation tangles were clearly visible. The interior damage which was comprised of dislocation loops after the dual temperature anneal had turned into a broader but more scattered band of small damage clusters covering a total distance of ~0.2 μm at 0.12 μm beneath the surface damage. Both the Cr and O profiles remained essentially the same (Fig. 14b). Besides a small increase in the magnitude of the last and most prominent Cr peak, a better match between the positions of Cr and O peaks was observed.

The increase in width of the surface damage band in the unannealed specimen demonstrated the increased radiation damage associated with a

higher oxygen implant dose. Due to the pinning effect of oxygen, longer annealing time and/or higher annealing temperature were required to fully recover from the implantation induced damage and restore lattice order. Though all implantation processes had been performed at room temperature, recrystallization had occurred as illustrated by the distinct spots in the ring pattern of the TED pattern. The implantation at high dose rate was suspected to have caused an elevation in temperature during the implantation. An in situ annealing of defects apparently occurred.

With a high fluence oxygen implant, the tremendous influence that damage had on Cr redistribution was significantly reduced at 600°C. Instead of a prominent Cr peak which corresponded to the interior damage band in the low dose samples, the concentration of Cr drastically diminished to a mere shoulder as oxygen concentration increased. Corresponding to pronounced Cr peaks, high oxygen concentration was detected.

The existence of a high oxygen concentration seemed to have caused a significant pinning effect on Cr atoms which were in the process of migrating towards the specimen surface or defect sites. The appearance of the most prominent Cr peak in the innermost position indicated that the following might be the case:

As Cr atoms out-diffused and encountered regions of high oxygen concentration at the higher annealing temperature, the chemical affinity between O and Cr may have caused the formation of stable Cr-oxygen complexes. The presence of oxygen in the deeper region had

therefore acted as a trap for Cr as far as its out-diffusion towards the specimen surface was concerned. This oxygen pinning action which prevented further Cr out-diffusion was probably responsible for the occurrence of the highest Cr peak in that region.

SUMMARY AND CONCLUSIONS

The as-implanted control sample contained a heavily damaged surface band. During annealing, this band evolved into dislocation tangles and a layer of small dislocation loops appeared before the band. The entire surface damage band disappearead at high annealing temperature and only a few single dislocation lines were left looping from the surface.

With 4×10^{13} cm^{-2} oxygen implant, more heavily damaged surface structures were obtained. The regrowth of the damaged region was substantially reduced as compared to that in the control sample. A thin layer of surface damage still persisted after the 840°C anneal.

The trend was more pronounced in the case of a higher dose oxygen implant (2×10^{15} cm^{-2}). Not only did the initial width of surface damage layer increase, but a broad band of damage still remained even after a 840°C anneal. The additional oxygen had retarded the recovery of implantation induced damage even after annealing at a temperature of 840°C for 15 minutes.

Cr segregation in the absence of any oxygen implantation showed good correlation with secondary damage distribution in the implanted region of the material. Cr peaks were always found corresponding to positions of residual damage after annealing.

With the introduction of a low dose oxygen, the influence of damage on Cr segregation became less obvious at low annealing temperature (600°C). A flattening of Cr peaks was observed. After annealing at higher temperature, Cr redistribution still correlated well with damage bands but the highest Cr peak shifted to the deeper damage band. The magnitude of the Cr peak tripled in the vicinity of this damage band.

The implantation of oxygen at a higher fluence resulted in pinning of Cr at 600°C. There was very little redistribution of Cr at 600°C. Its initial uniform distribution remained rather undisturbed. Only small fluctuations occurred at damage sites. After annealing O peaks appeared in regions of high defect concentration and Cr interaction with oxygen was observed. The highest Cr peak now coincided with the innermost oxygen peak and corresponded to the innermost band of damage.

The following conclusions can be drawn from the present experiments:

1. Room temperature implantation into GaAs under the conditions of this experiment did not produce a homogenous amorphous layer. The implanted region appeared to be heavily damaged with various defect structures. The crystallinity in the as-implanted material was evident from the presence of striations parallel to <111> in the cross-section TEM micrograph and was further supported by a definite single crystal spot pattern in the TED.
2. In the absence of oxygen, Cr segregation occurred at regions of high dislocation density.

3. When oxygen was implanted, the rate of recovery of implantation induced structural damage by furnace annealing decreased and Cr segregation towards damage sites was considerably suppressed at 600°C.
4. At temperatures above 800°C, Cr segregation at damage sites was enhanced. The highest Cr peak occurred at the deepest damage band where out diffusing Cr first encountered both oxygen and high dislocation density.
5. The results suggest that relatively stable complexes involving O and Cr were formed. However, no such complexes large enough to be detected by TEM were observed.

ACKNOWLEDGEMENT

I would like to express my heartfelt thanks to my advisor, Professor J. Washburn and to Dr. D. K. Sadana for their guidance, inspiration, and collaboration in this work. Particularly to Professor Washburn who has not exerted pressure of any kind throughout this work. His understanding and thoughtfulness is gratefully appreciated.

Special thanks to Professor Wu, Dr. M. Cross, and Dr. C. Y. Kung for their stimulating discussions and valuable advice on this work, and Dr. R. G. Wilson of Hughes Research Lab for the SIMS profiles.

I also wish to thank all my friends in Berkeley who have made my stay in this country a most meaningful and pleasant one.

I especially would like to thank Miss Margaret Lee, my best friend, for giving my son her love and guidance during my absence. And above all to my beloved son Raymond, whose existence triggered me to fight for this second chance in life.

This work was supported by the Director, Office of Energy Research, Office of Health and Environmental Research of the U.S. Department of Energy under Contract No. DE-AC03-76SF00098.

REFERENCES

1. J. Lindhard, M. Scharff and H. E. Schiott. Mat. Fys. Medd. Dan. Vid. Selsk. 33, No. 14 (1963).
2. Ion Implantation in Si-Applied Solid State Science, Vol. 5, 1975 (K. A. Pickar).
3. D. K. Sadana, C. W. Magee, M. Maenpaa, G. R. Booker, Appl. Phys. Lett. 37(7), 615 (1980).
4. D. K. Sadana, M. Strahman, J. Washburn, and G. R. Booker, J. Appl. Phys. 51(11), 5718 (1980).
5. N.A.G. Ahmed, G. Carter, C.E. Christodoulides, M. J. Nobes, and A. Titov, Nucl. Instr. Meth. 168, 283 (1980).
6. J. S. Williams and M. M. Austin, Appl. Phys. Lett. 36, 944 (1980).
7. D. K. Sadana, M. C. Wilson, G. R. Booker, and J. Washburn, J. Electrochem. Soc. 127, 1589 (1980).
8. D. K. Brice, "Ion Implantation", p. 101, Gordon and Breach, New York 1971, p. 101.
9. K. Seshan and J. Washburn, Radiation Effects 37, 147 (1978).
10. D. K. Sadana and G. R. Booker, Radiation Effects 42, 35 (1979).
11. J. Fletcher and G. R. Booker in the Proceedings of the 9th International Congress on Electron Microscopy Toronto 1978, Vol. 3, p. 364.
12. R. W. Bicknell, J. Micros. 98, 165 (1979).
13. M. L. Jenkins, D.J.H. Cockayne and M. J. Whelan, J. Micros, 98 155 (1979).
14. D. K. Sadana and G. R. Booker, Radiation Effects, 42, 35 (1979).

15. R. M. Drosd, PhD Thesis, University of California, Berkeley 1979, pp. 15-41, LBL report No. 9990.

16. J. F. Gibbons, Proc. IEEE 60, 1062 (1972).

17. S. M. Davidson and G. R. Booker, "Ion Implantation", p. 51.

18. R. W. Bicknell and R. M. Allen, "Ion Implantation", p. 63.

19. D. E. Davies and S. A. Roosild, Appl. Phys. Lett. 17, 107 (1970).

20. D. K. Sadana, J. Fletcher, and G. R. Booker, Electron Lett. 13, 632 (1977).

21. D. K. Sadana, G. R. Booker, B. J. Sealy, K. G. Stephens, and M. H. Badawi, Radiation Effects 183. (1980)

22. T. J. Magee, J. Peng., J. D. Hong, C. A. Evans, Jr., V. R. Deline, R. M. Malbon, Appl. Phys. Lett. 35, 277 (1979).

23. A. Masuyama, M. A. Nicolet, I. Golecki, J. L. Tandon, D. K. Sadana, and J. Washburn, Appl. Phys. Lett. 36, (1980).

24. R. G. Wilson, P. K. Vasudev, D. M. Jamba, C. A. Evans, Jr., and V. R. Deline, Appl. Phys. Lett 36, (1980).

25. P. N. Favennec and H. L. Haridon, Appl. Phys. Lett. 35, (1979).

26. P. K. Vasudev, R. G. Wilson and C. A. Evans, Jr., Appl. Phys. Lett. 37 (1980).

27. C. A. Evans, Jr., V. R. Deline, T. W. Sigmon, and A. Lidow, Appl. Phys. Lett. 35 (1980).

28. B. Tuck, G. A. Adegboyega, P. R. Jay, and M. J. Cardwell, "Gallium Arsenide and Related Compounds," (1978).

29. T. Noxaki, Mogawa, and H. Watanabe, Multi-layer epitaxial technology for the Schottky barrier GaAs field-effect transistor in Gallium Arsenide and Related Compounds, 1974 (Inst. Phys. Conf. Series No. 24, 1975).

30. T. J. Magee, J. Hong, V. R. Deline, and C. A. Evans, Jr., Appl. Phys. Lett. 37 (1980).

31. T. J. Magee, J. Peng., J. D. Hong, W. Katz, and C. A. Evans, Phys. Stat. Sol. 55, 161 (1979).

32. D. E. Newbury, Quantitative Surface analysis of Materials.

FIGURE CAPTIONS

Figure 1. (a) TEM plan view micrograph of self-implanted, unannealed sample.

(b) Cross-section micrograph of the same showing defect distribution.

Figure 2. (a) Cross-section micrograph showing defect distribution in the control sample after 15 min. anneal in N_2 at 600°C.

(b) Cr atom-depth distribution from the same sample.

Figure 3. (a) TEM plan view of same sample as in Fig. 2a and 2b.

(b) TEM plan view of high dose sample after 15 min. anneal at 600°C.

Figure 4. (a) Cross-section micrograph showing defect distribution in 600°C/40 min. annealed control sample.

(b) Cr atom distribution from the same sample.

Figure 5. (a) TEM plan view of control sample after 600°C/40 min. anneal in N_2.

(b) TEM plan view of control sample after 600°C/40 min. anneal in air.

FIgure 6. (a) Cross-section micrograph showing distribution of defects in the same sample as in Fig. 5b.

(b) Oxygen and Cr atom distribution curves from the same sample.

FIgure 7. (a) Cross-section micrograph showing discrete dislocation loops in the control sample annealed at 840°C for 15 min.

(b) Cr atom distribution from the same sample.

Figure 8. (a) Cross-section micrograph showing defect distribution in the low dose sample after annealing at 600°C for 15 minutes.

(b) Oxygen and Cr atom distributions from the same sample.

Figure 9. (a) Cross-section micrograph showing defect distribution in the low dose sample after annealing for 15 minutes at 600°C and again annealing for 15 minutes at 840°C.

(b) Oxygen and Cr atom distributions from the same sample.

Figure 10. (a) Cross-section micrograph showing a discrete layer of buried dislocation loops in the low dose sample after a 15 minute anneal at 840°C.

(b) Oxygen and Cr atom distributions from the same sample.

Figure 11. (a) TEM plan view of the unannealed high dose sample. Inset is the TED diffraction pattern taken from a thin area of the same sample.

(b) Cross-section micrograph from the same sample.

Figure 12. (a) Oxygen atomic distribution profile from the high dose samples before and after annealing at 600°C/15 min., plus 840°C/15 min.

Figure 13. (a) Cross-section TEM micrograph of the high dose sample after annealing for 15 minutes at 600°C.

(b) Oxygen and Cr atom distributions from the same sample.

Figure 14. (a) Cross-section micrograph showing defect distribution in the same sample as in Fig. 13a and b, but further annealed for another 15 minutes at 840°C.

(b) Oxygen and Cr atom distributions from the same sample.

Figure 15. (a) Cross-section micrograph of high dose sample after annealing for 15 minutes at 840°C.

(b) Oxygen and Cr atom distributions from the same sample.

Figure 16. Cr atom distribution in the control samples, unannealed, annealed for 15 minutes at 600°C, and annealed for 15 minutes at 840°C, respectively.

Figure 17. Hypothetical distribution of ion concentration versus depth during ion implantation.

Figure 18. Comparison between theoretcial profile of damage and experimental ion distribution for 80 keV and 150 keV B^+ in Si.

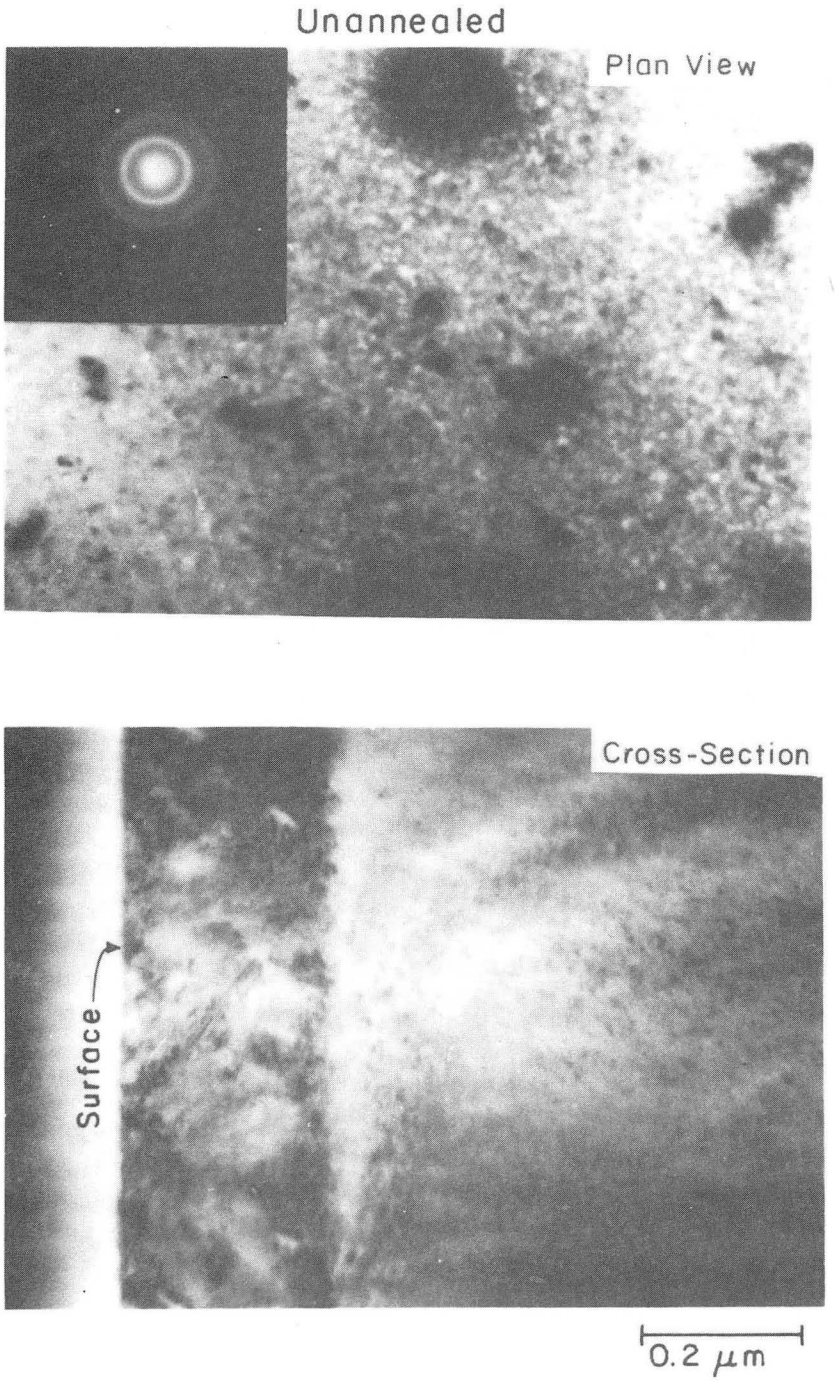

XBB 818-8082

Figure 1.

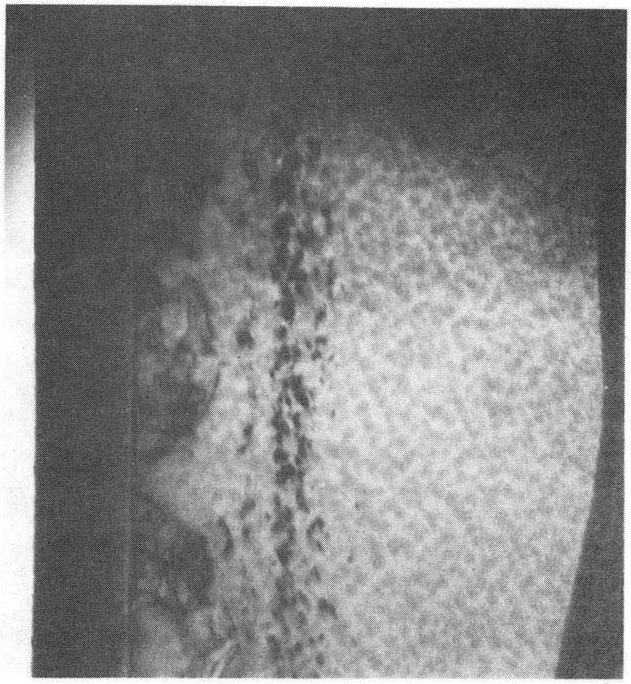

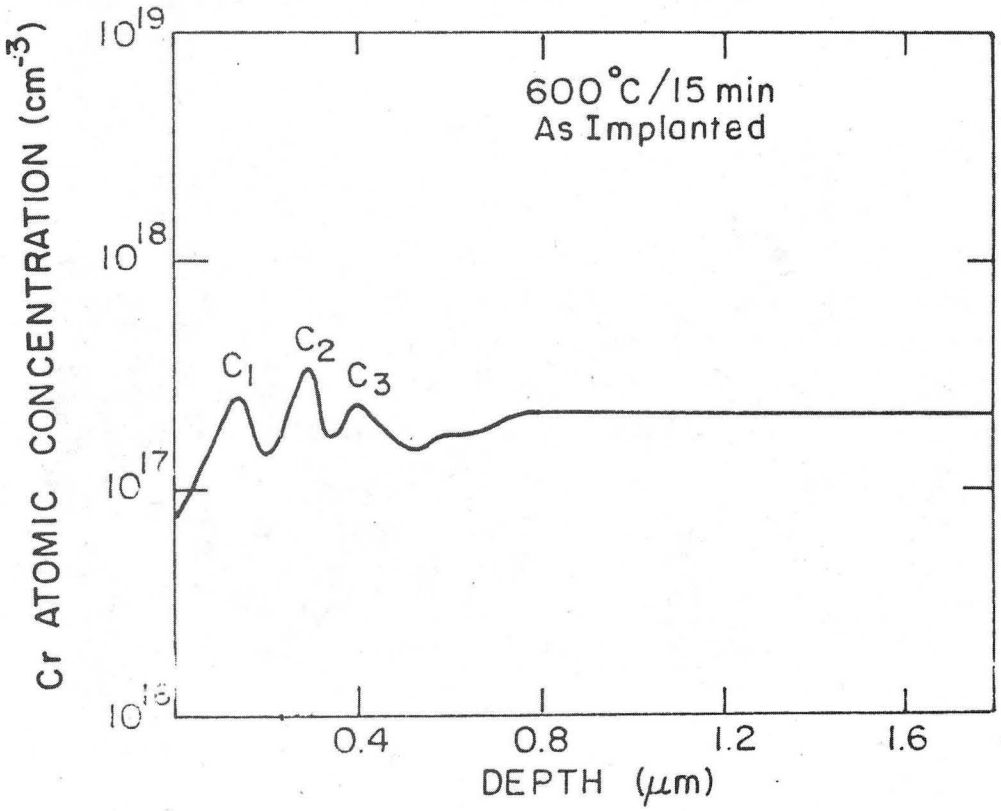

XBB 820-10591

Figure 2.

TEM PLAN VIEW MICROGRAPHS
OF SELF-IMPLANTED (100) GaAs

600°C / 15 min.

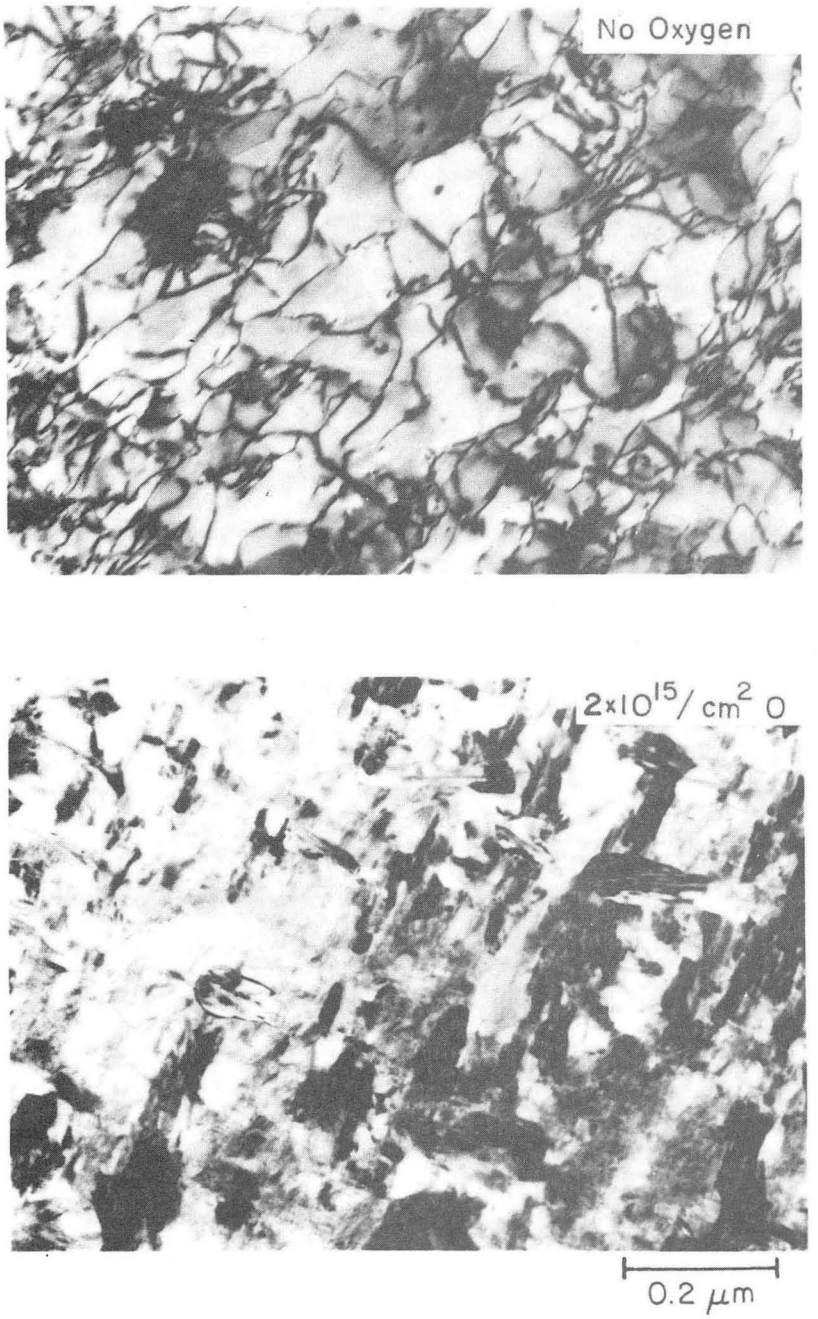

XBB 818-8079

Figure 3.

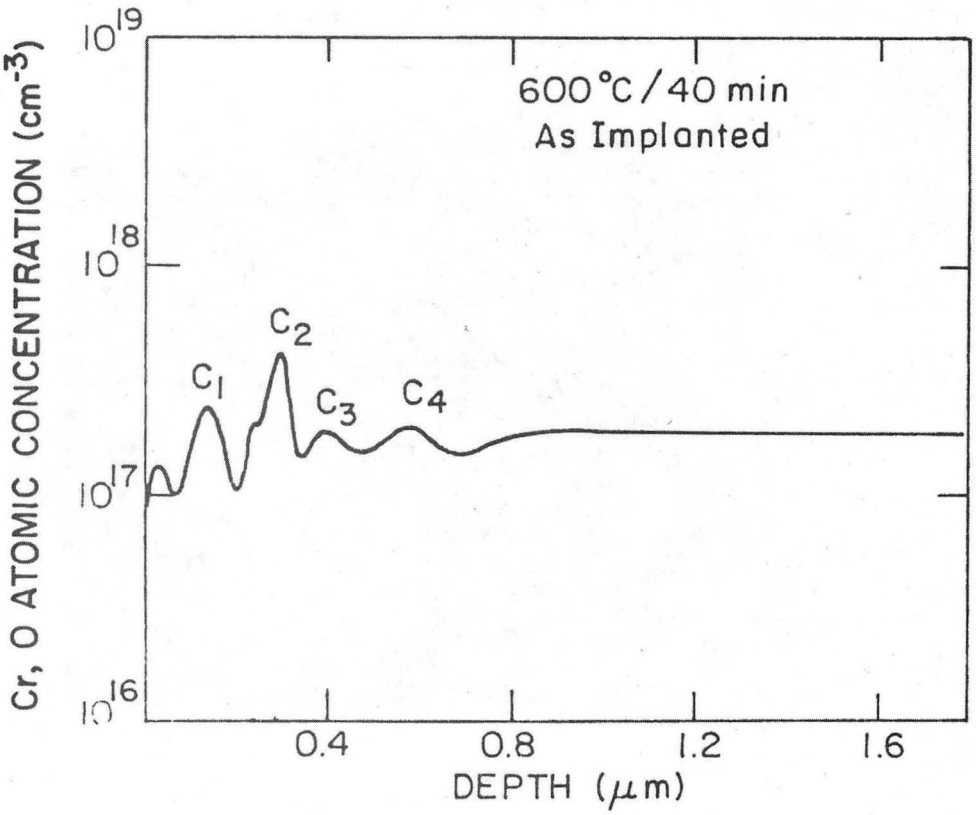

XBB 820-10590

Figure 4.

TEM PLAN VIEW MICROGRAPHS
OF SELF-IMPLANTED (100) GaAs

600°C/40 min.

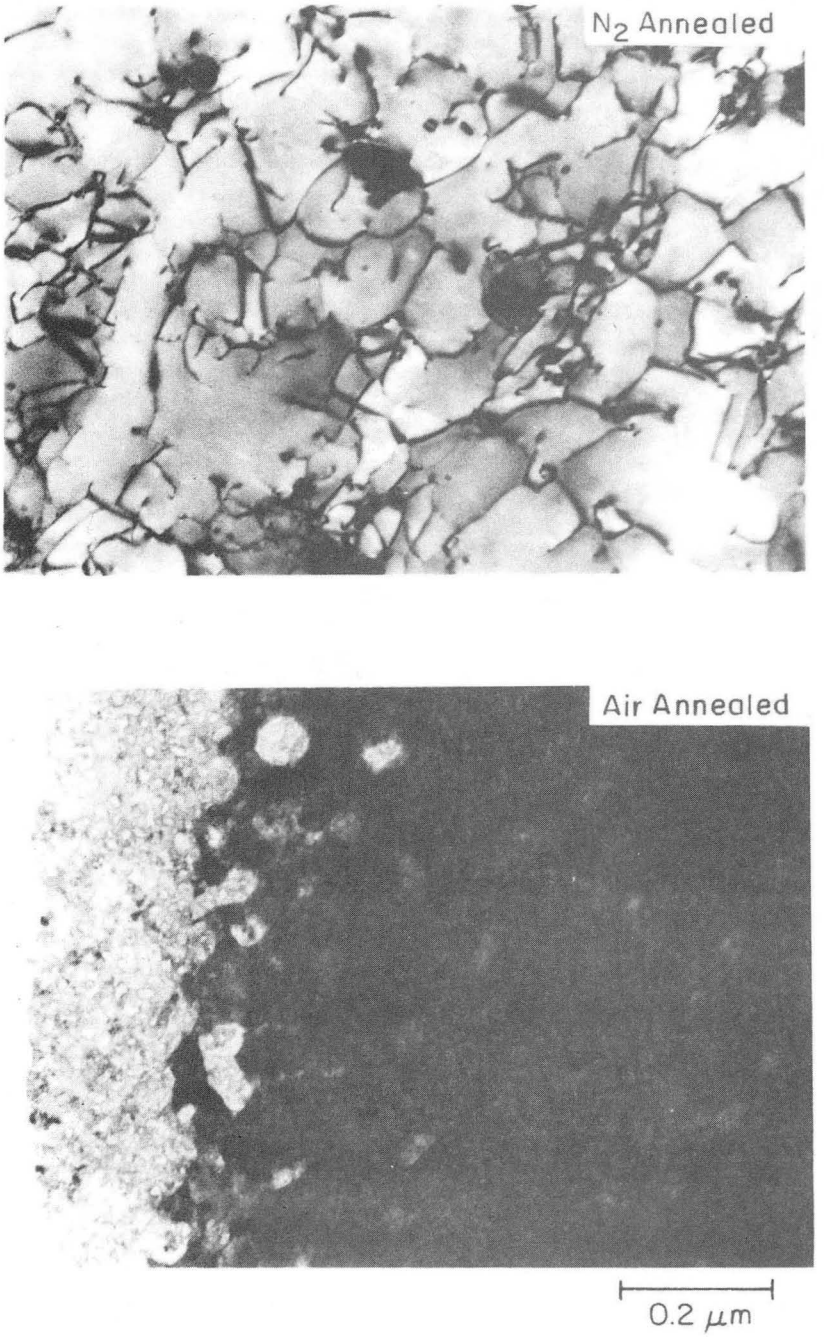

XBB 818-8080

Figure 5.

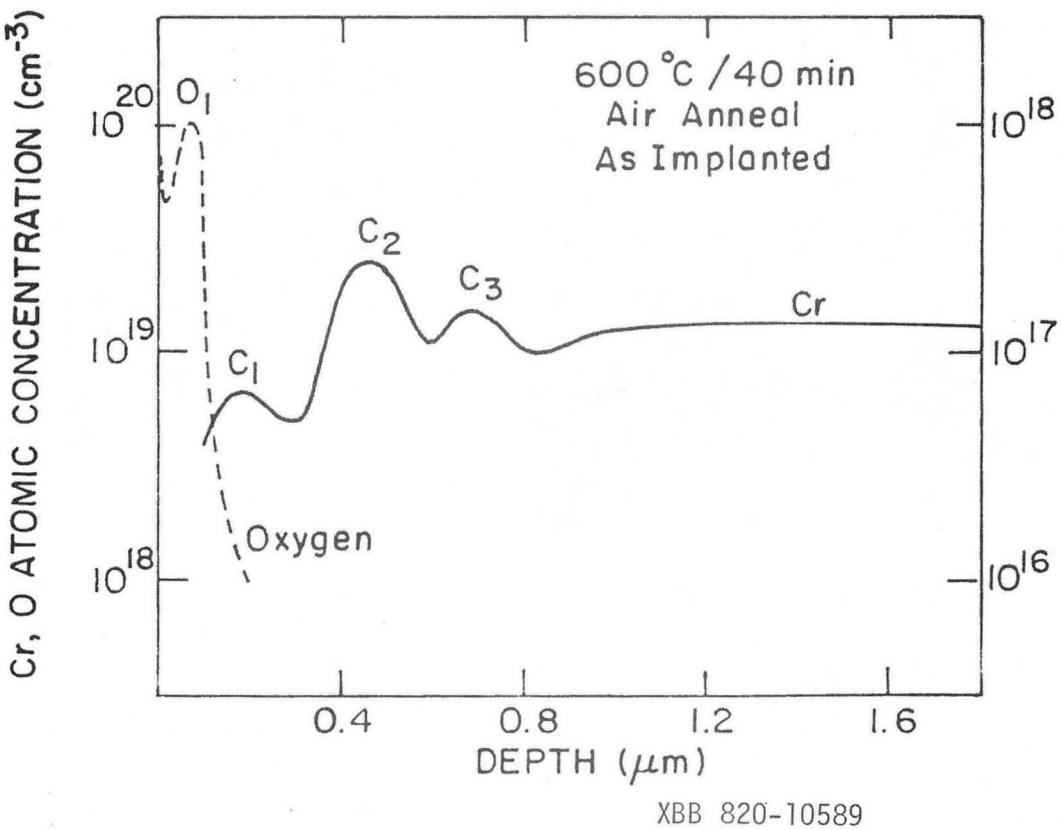

XBB 820-10589

Figure 6.

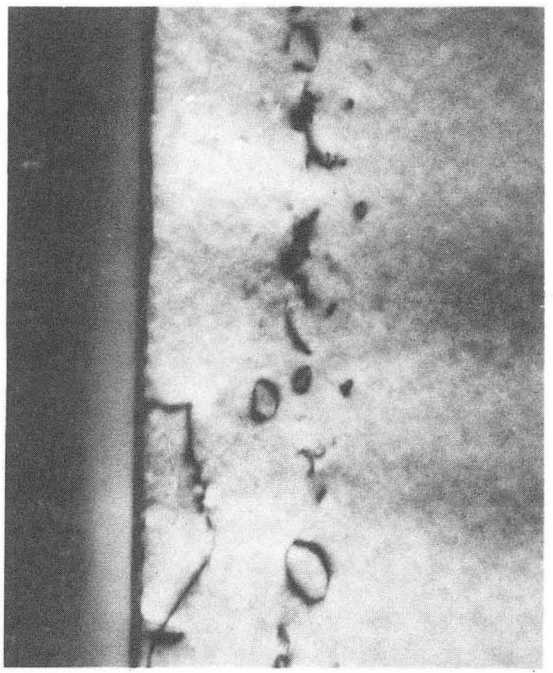

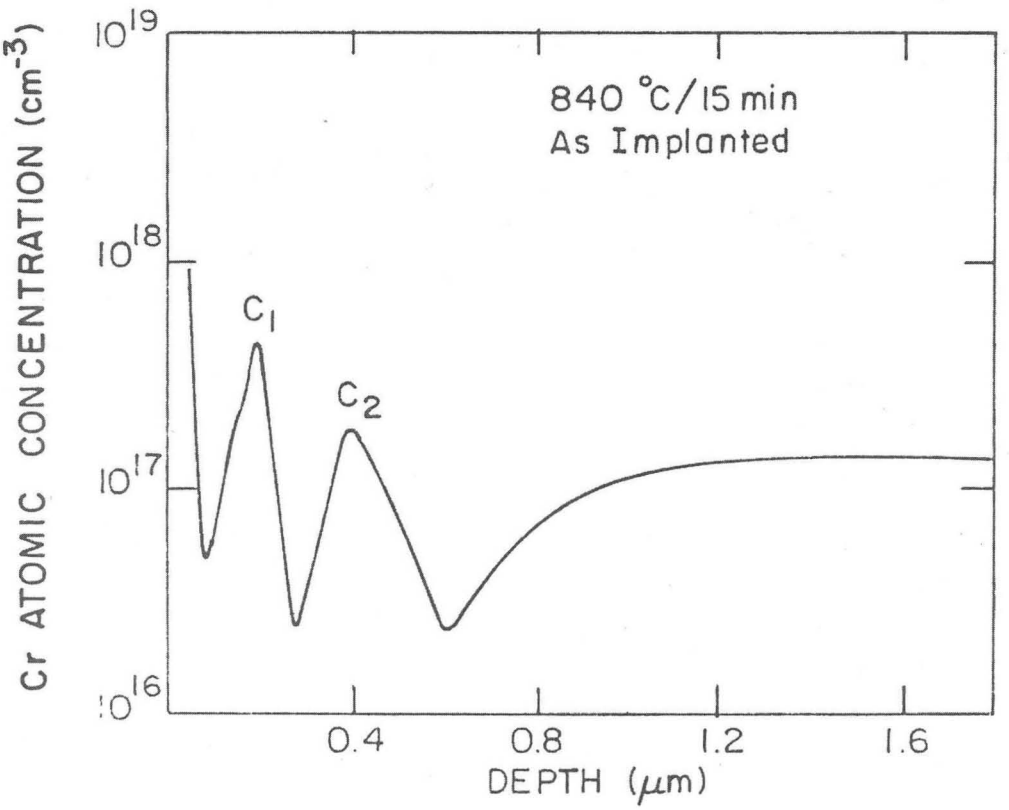

XBB 820-10588

Figure 7.

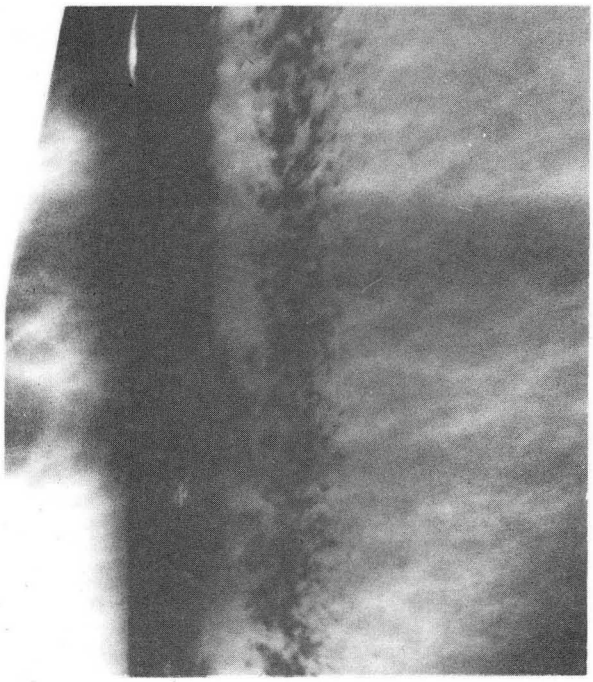

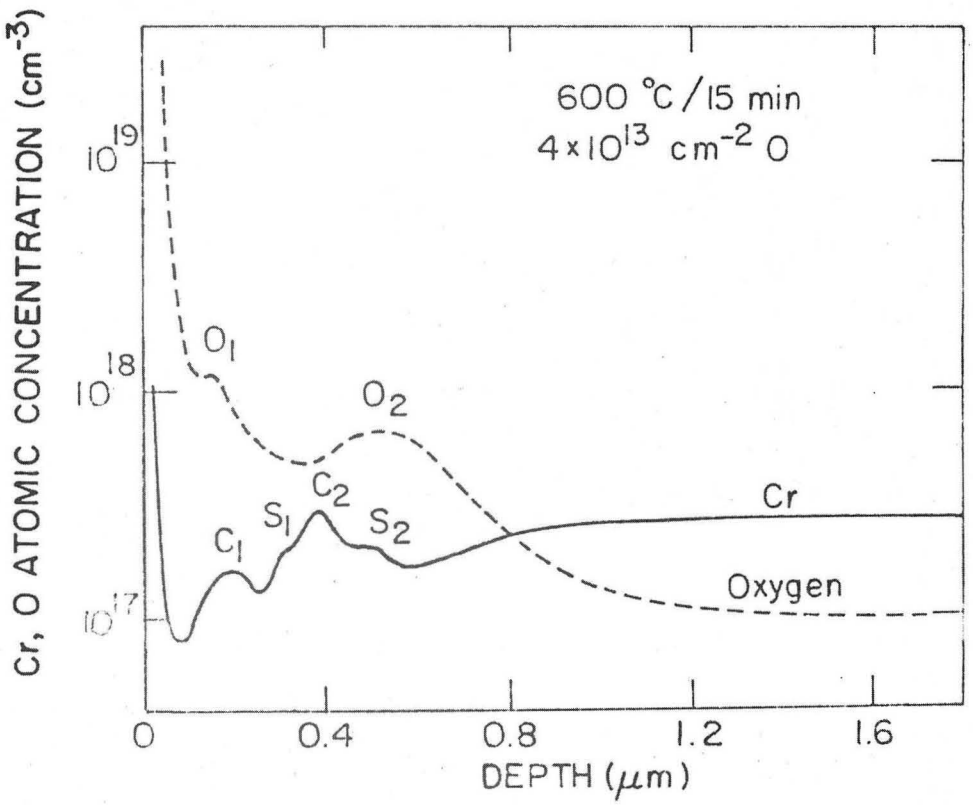

XBB 820-10587

Figure 8.

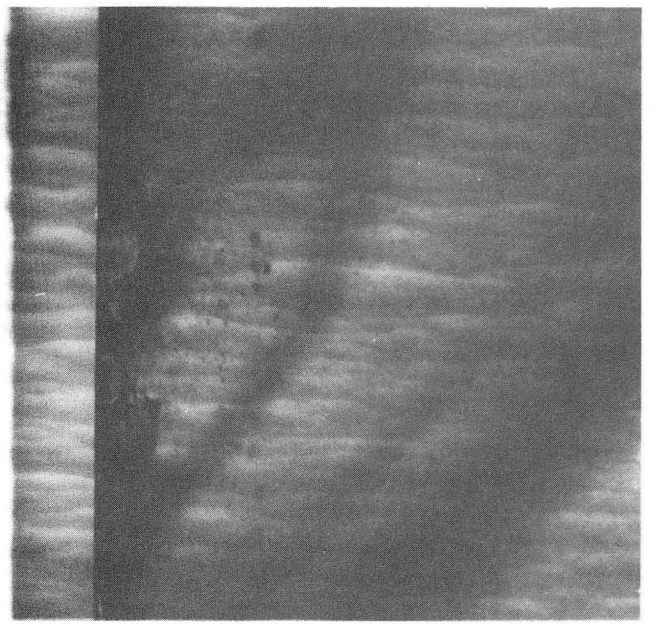

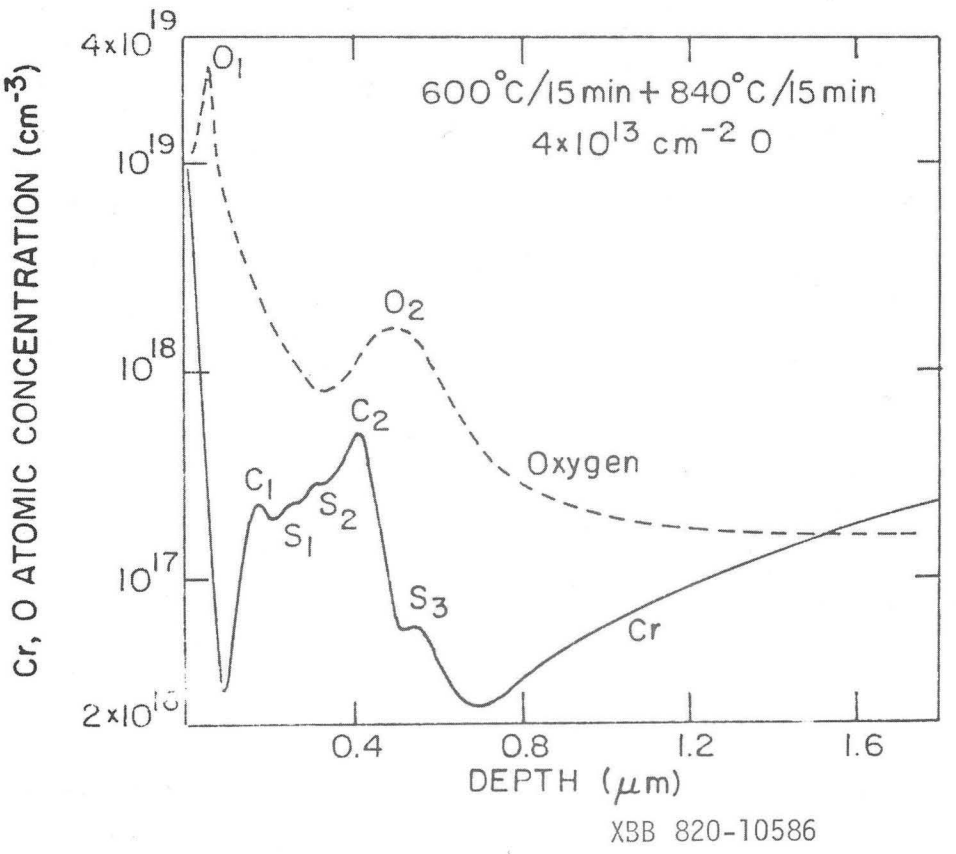
Cr, O ATOMIC CONCENTRATION (cm^{-3})
4x10^{19}
10^{19}
10^{18}
10^{17}
2x10^{16}
600°C/15 min + 840°C/15 min
4x10^{13} cm^{-2} O
O$_1$
O$_2$
C$_1$
C$_2$
S$_1$
S$_2$
S$_3$
Oxygen
Cr
0.4
0.8
1.2
1.6
DEPTH (μm)
XBB 820-10586

Figure 9.

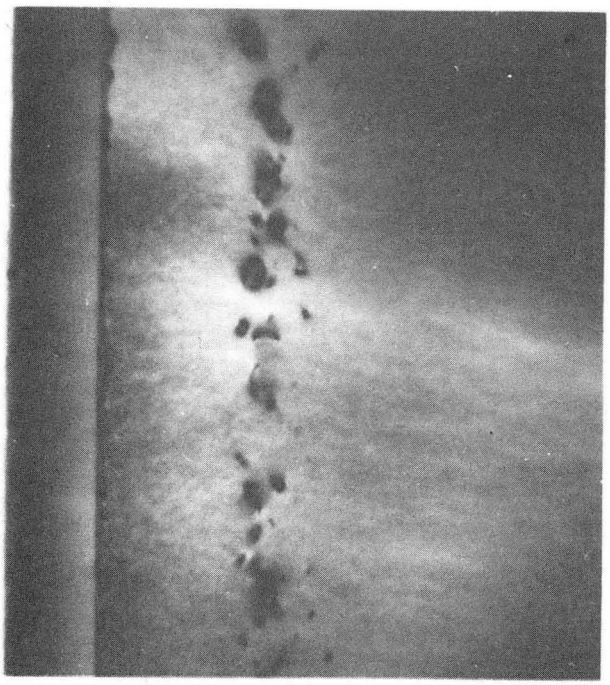

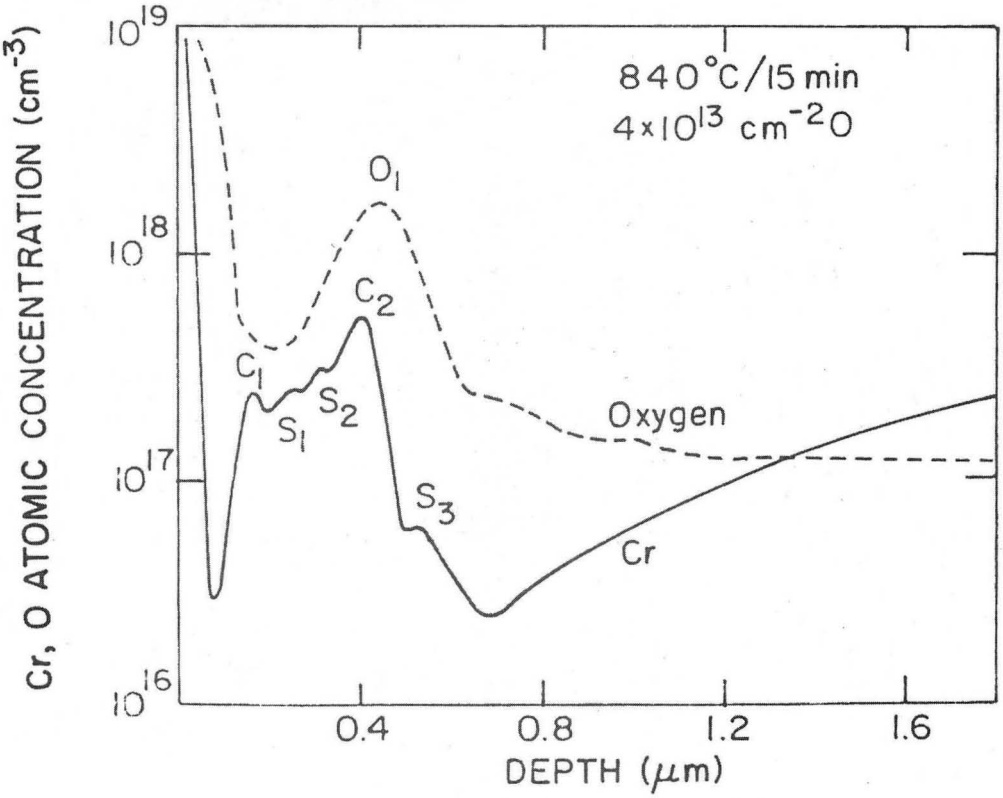

XBB 820-10585

Figure 10.

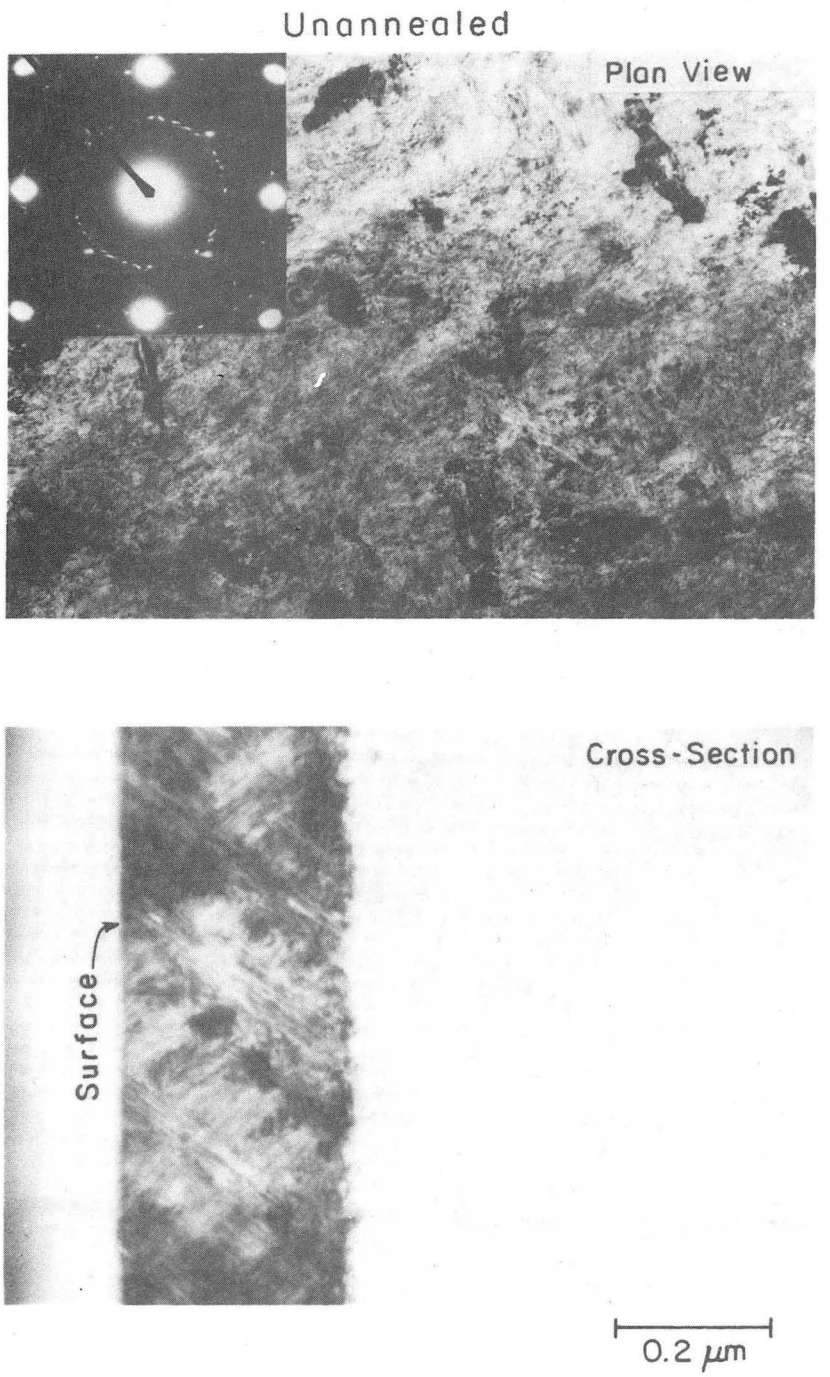
(SELF + O) IMPLANTED GaAs
Unannealed
Plan View
Cross-Section
Surface
0.2 μm
XBB 818-8081

Figure 11.

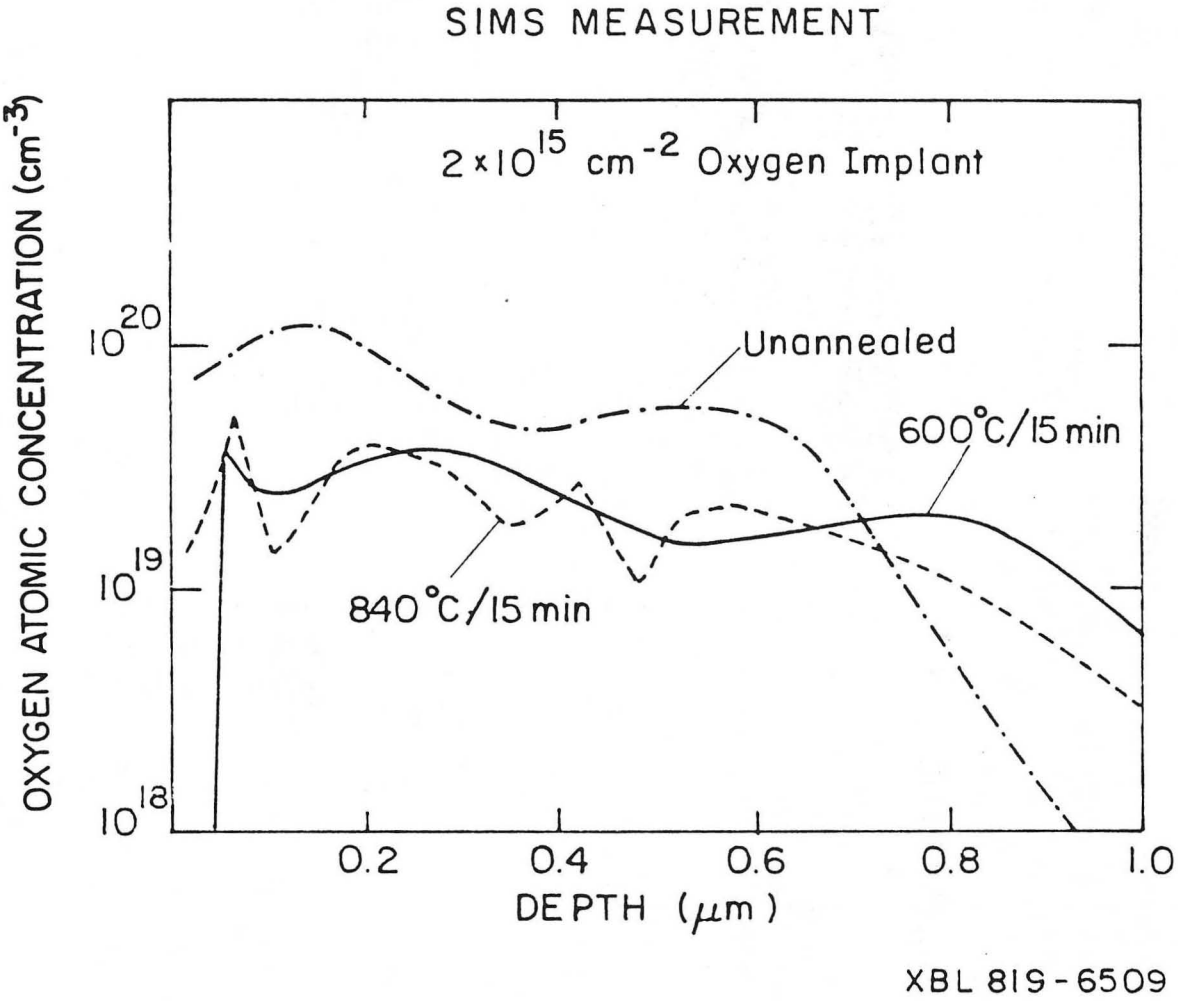
SIMS MEASUREMENT
2×10^15 cm^-2 Oxygen Implant
Unannealed
600°C/15 min
840°C/15 min
OXYGEN ATOMIC CONCENTRATION (cm^-3)
10^20
10^19
10^18
0.2
0.4
0.6
0.8
1.0
DEPTH (μm)
XBL 819-6509

Figure 12.

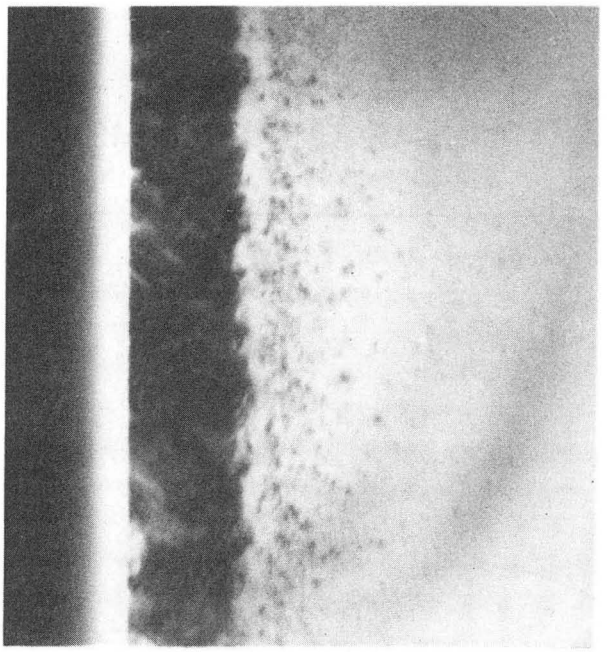

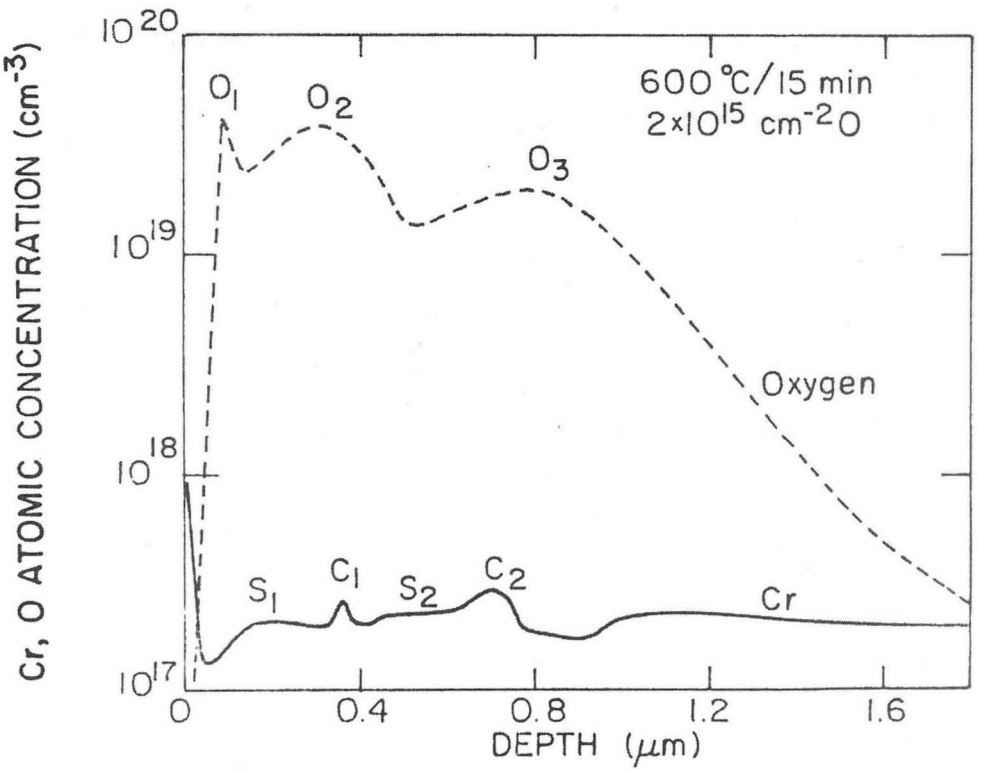

XBB 820-10594

Figure 13.

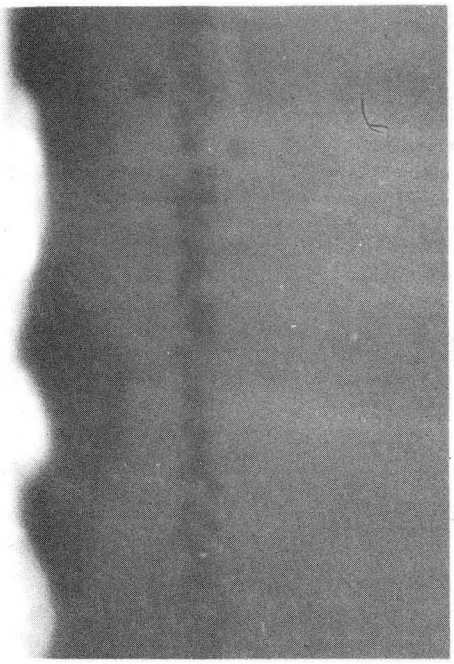

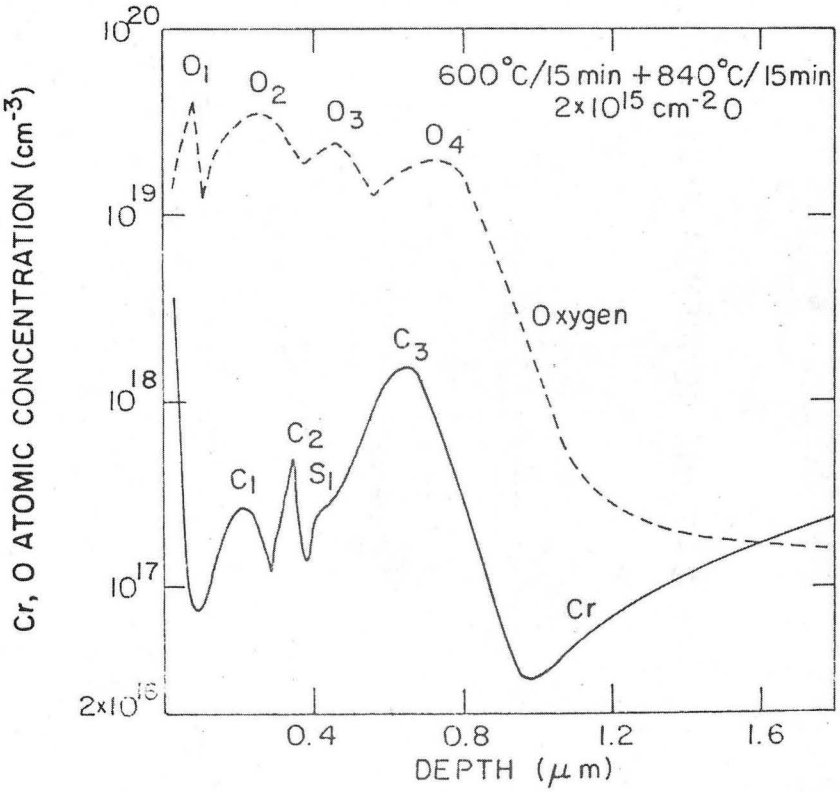

XBB 820-10593

Figure 14.

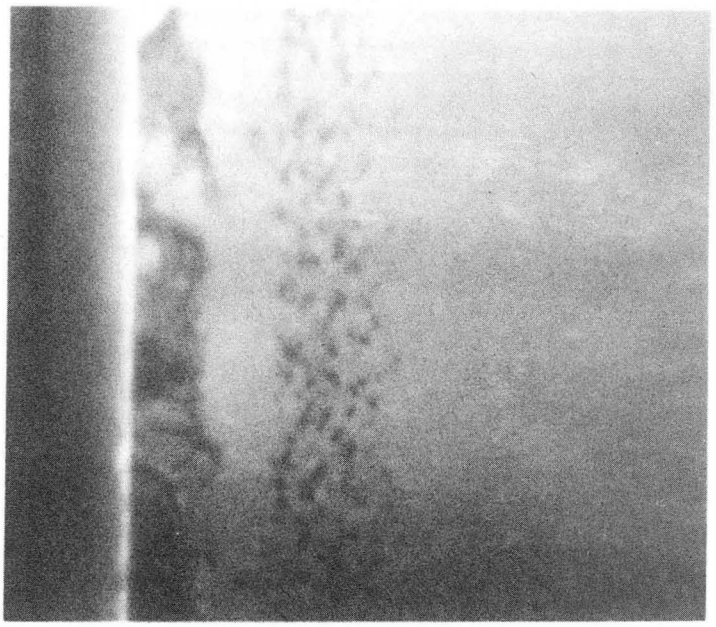

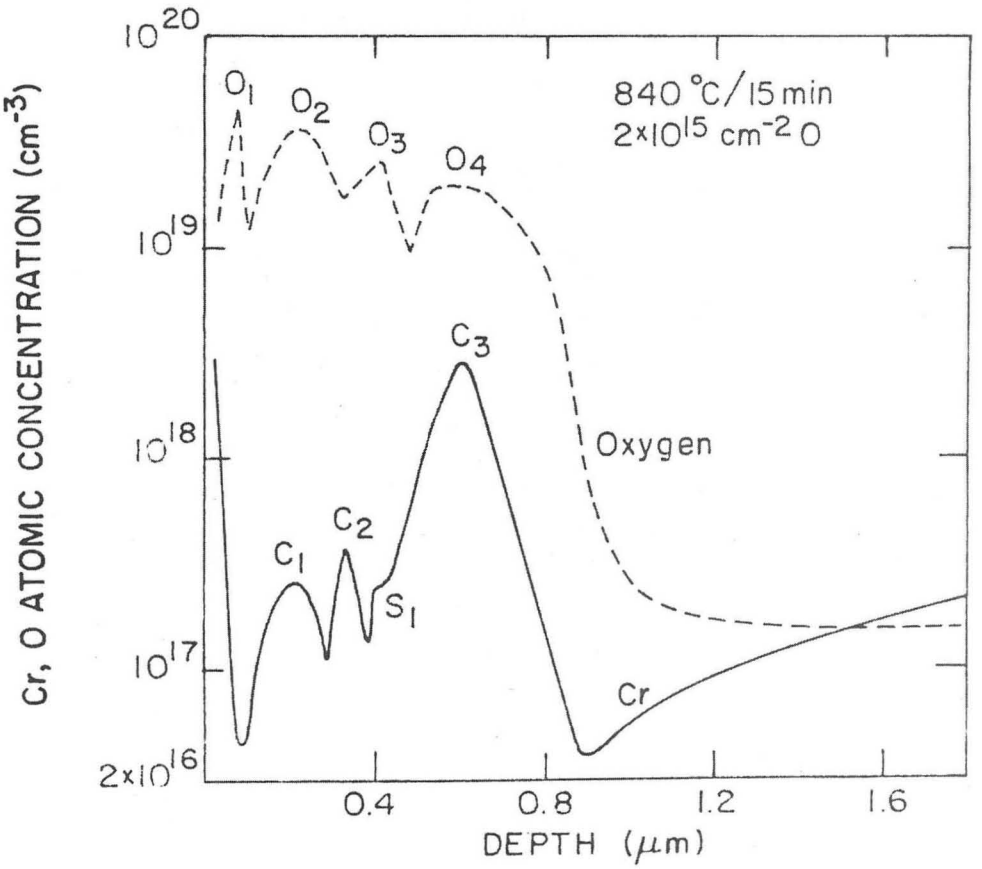

XBB 820-10592

Figure 15.

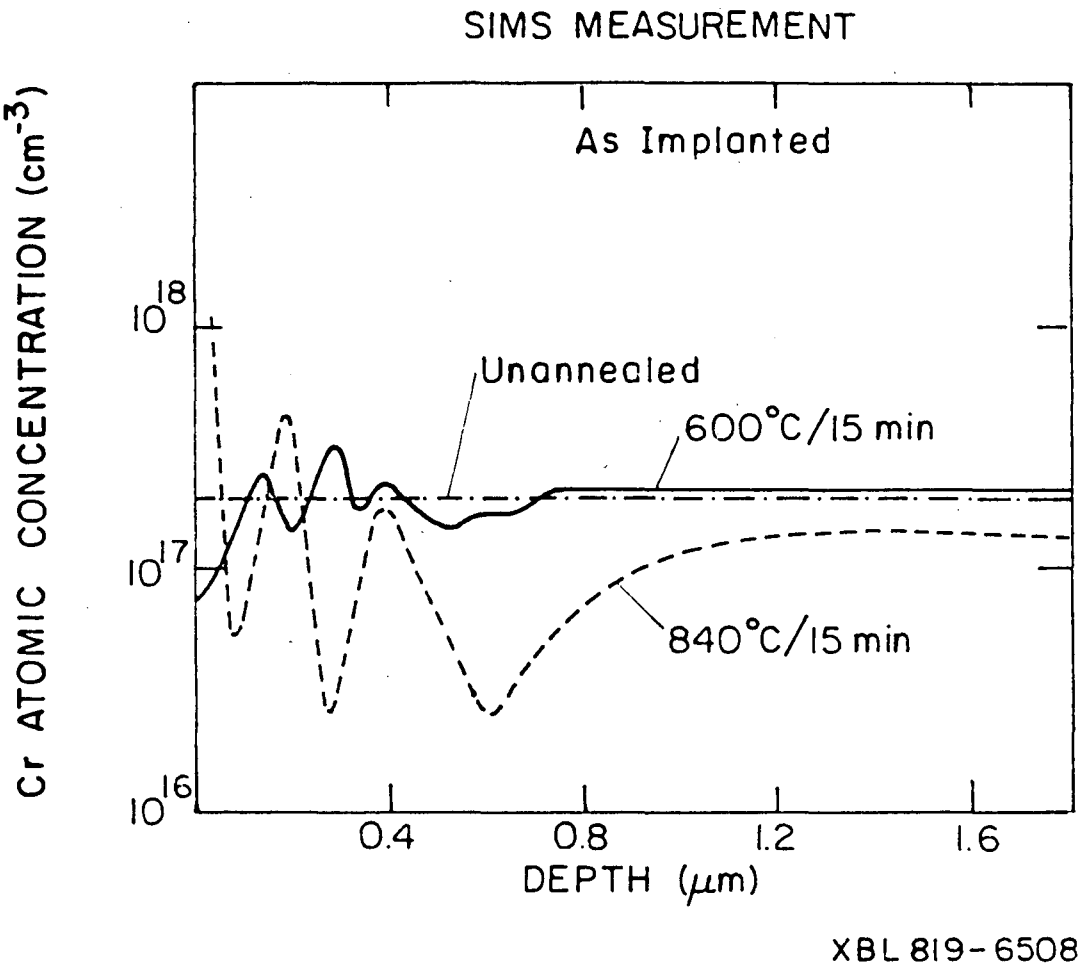
SIMS MEASUREMENT
As Implanted
Unannealed
600°C/15 min
840°C/15 min
Cr ATOMIC CONCENTRATION (cm^{-3})
10^{18}
10^{17}
10^{16}
0.4
0.8
1.2
1.6
DEPTH (μm)
XBL 819-6508

Figure 16.

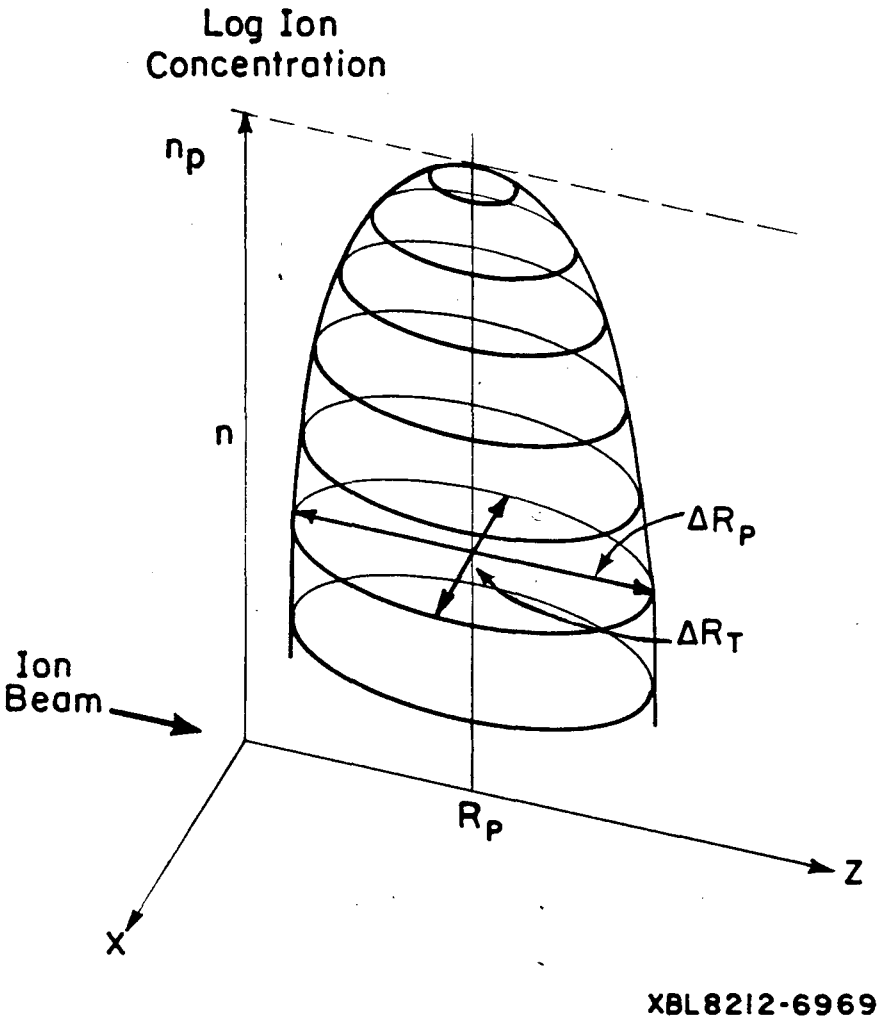
Log Ion
Concentration
n_p
n
ΔR_p
ΔR_T
Ion
Beam
R_p
Z
X
XBL8212-6969

Figure 17.

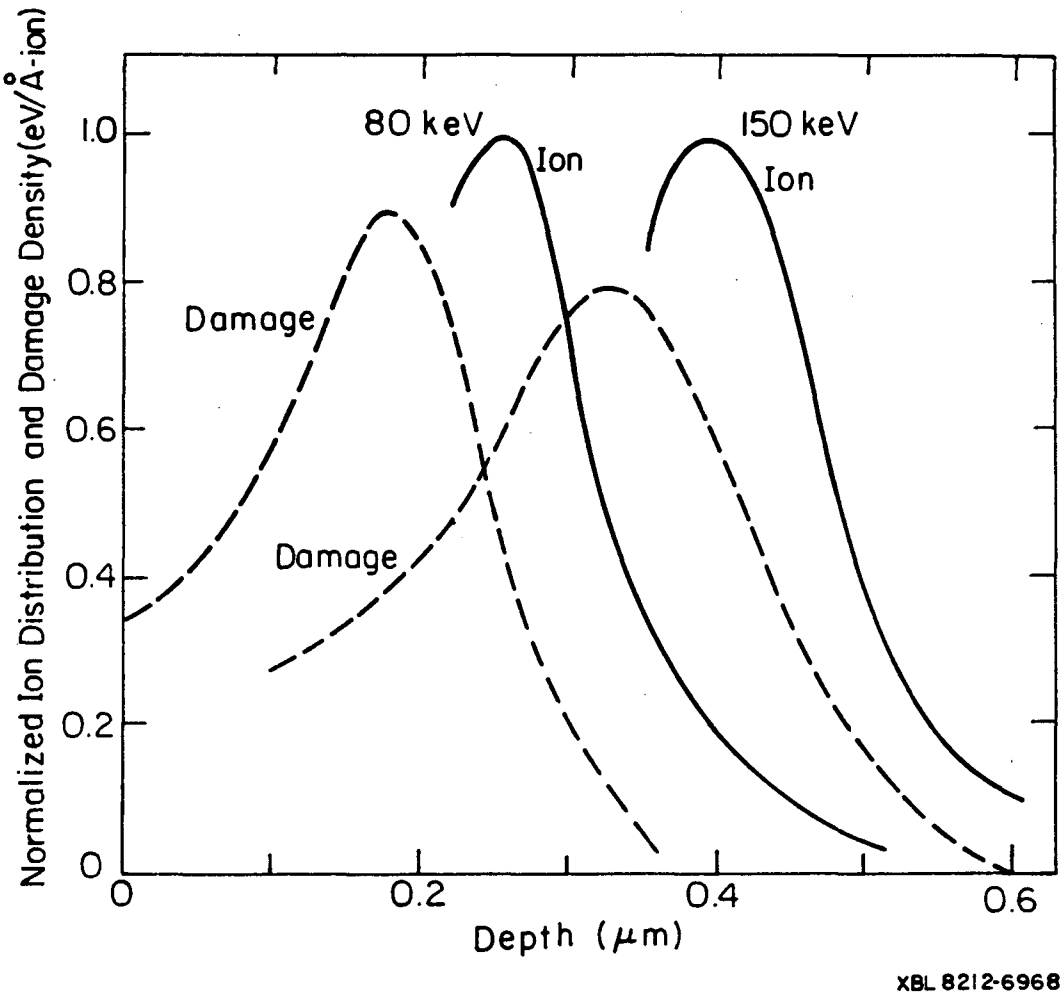
Normalized Ion Distribution and Damage Density(eV/Å-ion)
1.0
0.8
0.6
0.4
0.2
0
0
0.2
0.4
0.6
Depth (μm)
80 keV
Ion
150 keV
Ion
Damage
Damage
XBL 8212-6968

Figure 18.

This report was done with support from the Department of Energy. Any conclusions or opinions expressed in this report represent solely those of the author(s) and not necessarily those of The Regents of the University of California, the Lawrence Berkeley Laboratory or the Department of Energy.

Reference to a company or product name does not imply approval or recommendation of the product by the University of California or the U.S. Department of Energy to the exclusion of others that may be suitable.

TECHNICAL INFORMATION DEPARTMENT
LAWRENCE BERKELEY LABORATORY
UNIVERSITY OF CALIFORNIA
BERKELEY, CALIFORNIA 94720